The Astronomical Journal, 149:193 (11pp), 2015 June doi:10.1088/0004-6256/149/6/193

H II REGION G46.5-0.2: THE INTERPLAY BETWEEN IONIZING RADIATION, MOLECULAR GAS, AND STAR FORMATION

S. Paron[1,2], M. E. Ortega[1], G. Dubner[1], Jing-Hua Yuan [3], A. Petriella[1], E. Giacani[1,2], Jin Zeng Li[3], Yuefang Wu[4], Hongli Liu[3], Ya Fang Huang[3], and Si-Ju Zhang[3]
[1] Instituto de Astronomía y Física del Espacio (IAFE, CONICET-UBA), CC 67, Suc. 28, 1428 Buenos Aires, Argentina; sparon@iafe.uba.ar
[2] FADU—Universidad de Buenos Aires, Ciudad Universitaria, Buenos Aires, Argentina
[3] National Astronomical Observatories, Chinese Academy of Sciences, 20 A Datun Road, Chaoyang District, Beijing 100012, China
[4] Department of Astronomy, Peking University, 100871 Beijing, China
Received 2014 October 23; accepted 2015 April 14; published 2015 May 21

ABSTRACT

H II regions are particularly interesting because they can generate dense layers of gas and dust, elongated columns or pillars of gas pointing toward the ionizing sources, and cometary globules of dense gas where triggered star formation can occur. Understanding the interplay between the ionizing radiation and the dense surrounding gas is very important to explain the origin of these peculiar structures, and hence to characterize triggered star formation. G46.5-0.2 (G46), a poorly studied galactic H II region located at about 4 kpc, is an excellent target for performing this kind of study. Using public molecular data extracted from the Galactic Ring Survey (^{13}CO $J = 1$–0) and from the James Clerk Maxwell Telescope data archive (^{12}CO, ^{13}CO, C^{18}O $J = 3$–2, HCO$^+$, and HCN $J = 4$–3), and infrared data from the GLIMPSE and MIPSGAL surveys, we perform a complete study of G46, its molecular environment, and the young stellar objects (YSOs) placed around it. We found that G46, probably excited by an O7V star, is located close to the edge of the GRSMC G046.34-00.21 molecular cloud. It presents a horse-shoe morphology opening in the direction of the cloud. We observed a filamentary structure in the molecular gas likely related to G46 and not considerable molecular emission toward its open border. We found that about 10′ to the southwest of G46 there are some pillar-like features, shining at 8 μm and pointing toward the H II region open border. We propose that the pillar-like features were carved and sculpted by the ionizing flux from G46. We found several YSOs likely embedded in the molecular cloud grouped in two main concentrations: one, closer to the G46 open border consisting of Class II type sources, and another mostly composed of Class I type YSOs located just ahead of the pillar-like features, strongly suggesting an age gradient in the YSO distribution.

Key words: H II regions – ISM: clouds – ISM: molecules – stars: formation

1. INTRODUCTION

Massive stars play a key role in the evolution of the Galaxy. They are the principal source of heavy elements and UV radiation. Through the combination of winds, massive outflows, expanding H II regions, and supernova explosions, they provide an important source of mixing turbulence in the interstellar medium (ISM). H II regions are particularly interesting because they can trigger the formation of a new generation of stars. Processes such as "collect and collapse" (e.g., Elmegreen et al. 1995) and radiative driven implosion (RDI; e.g., Bertoldi 1989) have been convincingly demonstrated to occur around H II regions, leading to the formation of stars (e.g., Thompson et al. 2004a; Deharveng et al. 2008; Zavagno et al. 2010; Paron et al. 2011; Dirienzo et al. 2012; Ortega et al. 2013). These processes generate dense layers of gas and dust at the interface between the H II regions and their parent molecular cloud, elongated columns (pillars) of gas pointing toward the ionizing sources, and cometary globules of dense gas (Tremblin et al. 2013). Understanding the interplay between the ionizing radiation and the dense surrounding gas is very important for explaining the origin of these peculiar structures, and hence for characterizing triggered star formation.

G46.5-0.2 (hereafter G46) is a poorly studied H II region about 8′ in size located at R.A. = $19^h17^m26^s$, decl. = 11°55′54″ (J2000), on the border of the molecular cloud cataloged as GRSMC G046.34-00.21 (Rathborne et al. 2009). Lockman (1989) observed a recombination line at $v_{LSR} \sim 57.2$ km s^{-1} toward this region. Kuchar & Bania (1994) detected H I absorption features up to 56.6 km s^{-1} and based on kinematical considerations proposed for this H II region a near distance of 3.8 kpc, while Quireza et al. (2006), using the same techniques, favored a far distance of 7.8 kpc. Finally, Anderson & Bania (2009) resolved the kinematic distance ambiguity for G46 based on existing HI and ^{13}CO sky surveys, confirming a near distance of 4 kpc, which will be adopted the following.

Figure 1 shows a two-color composite image of the G46 field where the *Spitzer*-IRAC 8 μm emission distribution is displayed in cyan and the *Spitzer*-MIPSGAL at 24 μm is displayed in red. The emission displayed in cyan mainly corresponds to radiation originated in polycyclic aromatic hydrocarbon (PAH) molecules. The far-UV photons leaking from the H II region excite the PAHs, which then emit in the mid-infrared. This emission encircles the 24 μm emission (in red) that arises from very small dust grains which are heated but not destroyed by the UV photons. The emission at 8 μm has a horse-shoe morphology, being thicker and more intense in the east-northeast direction and open to the southwest where it dilutes into the surrounding medium. In precisely the southwest direction, about 10′ away from G46, there are pillar-like features shining at 8 μm. In this paper, we explore the interrelationship among the H II region G46, the environmental conditions, and the young stellar objects (YSOs) in the region, underscoring evidence of triggered stellar formation in the immediate vicinity of G46 and beyond.

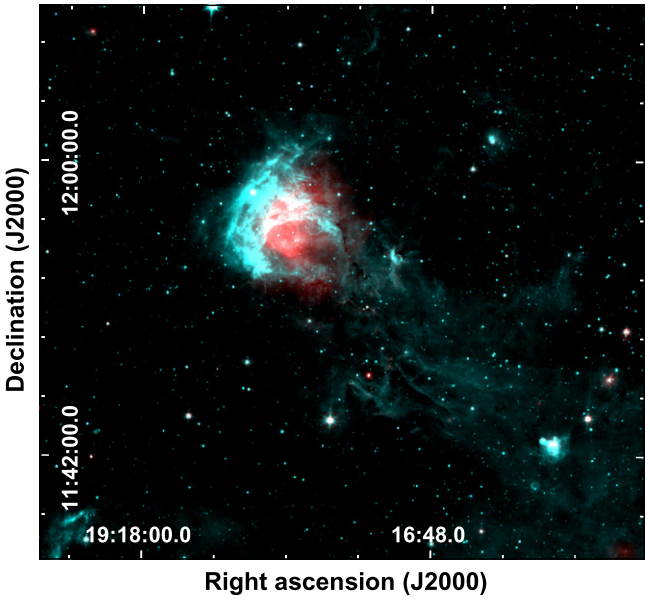

Figure 1. Two-color composite image of a large area toward the H II region G46. The *Spitzer*-IRAC 8 μm emission is shown in cyan, and the *Spitzer*-MIPSGAL emission at 24 μm is shown in red.

2. DATA

2.1. Molecular Data

The ^{13}CO $J = 1$–0 data were extracted from the Galactic Ring Survey (GRS). The survey, performed by Boston University and the Five College Radio Astronomy Observatory, maps the Galactic Ring in the mentioned molecular line with angular and spectral resolutions of 46″ and 0.2 km s^{-1}, respectively (see Jackson et al. 2006). The observations were performed in both the position-switching and on-the-fly mapping modes, achieving an angular sampling of 22″. Data are presented in the main beam temperature ($T_{\rm mb}$).

Additionally, we used ^{12}CO, ^{13}CO, C^{18}O $J = 3$–2, and HCO$^+$, HCN $J = 4$–3 data extracted from the James Clerk Maxwell Telescope (JCMT) data archive.[5] These observations (Proposal I.D M10AH02, P. I. Jonathan Williams) were carried out at the JCMT in Mauna Kea, Hawaii, using the HARP-ACSIS instrument. The angular and spectral resolutions were about 15″ and 0.05 km s^{-1}. We used the reduced data (cal. level 2), which were reduced using the standard ORAC-DR pipelines.[6] Data are presented in units of corrected antenna temperature T_A^*, which is related to the main beam temperature ($T_{\rm mb}$) using $T_{\rm mb} = T_A^*/\eta_{\rm mb}$. Following Buckle et al. (2009), a value of $\eta_{\rm mb} = 0.6$ was used. The zenith opacity was between 0.04 and 0.06 for all of the observed lines. Even though we extracted reduced data, in the case of the C^{18}O $J = 3$–2, HCO$^+$, and HCN $J = 4$–3 data, we applied a Hanning smoothing to improve the signal-to-noise ratio which altered the spectral resolution by no more than a factor of 2, and minor polynomials were used for baseline corrections using XSpec.[7]

[5] www.jach.hawaii.edu/JCMT/archive/

[6] http://www.jach.hawaii.edu/JCMT/archive/CADC_quickguide.html

[7] XSpec is a spectral line reduction package for astronomy which has been developed by Per Bergman at Onsala Space Observatory.

2.2. Infrared Data

In this work, archived infrared data are also used to reveal star formation in G46. These data come from the GLIMPSE (Galactic Legacy Infared Mid-Plane Survey Extraodinaire) and MIPSGAL surveys.

GLIMPSE (Benjamin et al. 2003), using the InfraRed Array Camera (IRAC; Fazio et al. 2004) on board the *Spitzer Space Telescope* (Werner et al. 2004), surveyed the inner 130° of the Galactic Plane in the 3.6, 4.5, 5.8, and 8.0 μm bands. The 5σ sensitivities of the four bands are 0.2, 0.2, 0.4, and 0.4 mJy, respectively. In addition to images, the GLIMPSE survey performed point-source photometry. Photometric data in the J (1.25 μm), H (1.65 μm), and Ks (2.17 μm) bands from the 2MASS Point Source Catalog (2MASS PSC; Skrutskie et al. 2006) are provided in the GLIMPSE Catalog to build up a 7 band photometric system. Both the images and the catalog of GLIMPSE are publicly available at the InfraRed Science Archive (IRSA),[8] where we retrieved cutouts in the four IRAC bands and point sources in a 31′ × 24′ region centered at $\alpha_{2000} = 19^{\rm h}17^{\rm m}18\overset{\rm s}{.}7$, $\delta_{2000} = +11°52'22\overset{''}{.}9$. We restricted the extracted catalog to be a more reliable data set using the following criteria: (a) only sources with photometric errors no larger than 0.2 MAG in the IRAC bands are taken into account; (b) for the 2MASS bands, a threshold of 0.1 MAG photometric error is used to eliminate unreliable photometric values. The photometric errors for IRAC and 2MASS sources were adopted following Gutermuth et al. (2009).

MIPSGAL (Carey et al. 2009) complements the GLIMPSE legacy survey. This survey, using the Multiband Infrared Photometer for *Spitzer* (MIPS; Rieke et al. 2004) instrument on board the *Spitzer Space Telescope*, surveyed an area comparable to that of GLIMPSE. Version 3.0 of the MIPSGAL data includes mosaics only at 24 μm with sky coverage of $|b| < 1°$ for $-68° < l < 69°$ and $|b| < 3°$ for $-8° < l < 9°$. The spatial resolution and 5σ sensitivity at 24 μm are 6″ and 1.7 mJy. From the IRSA server, we extracted a cutout of a region similar to that of the GLIMPSE cutouts.

We conducted point-source extraction and aperture photometry of point sources in the MIPS 24 μm image using the point-spread function (PSF) fitting capability of IRAF/DAOPHOT (Stetson 1987). The PSF was determined to be about 6″ by fitting the profiles of 10 bright point sources in the investigated field. The standard deviation (σ) of the sky was estimated to be about 5.0×10^{-6} Jy pixel^{-1}. DAOFIND was used to extract candidates of point sources with a threshold of 10σ. The final sources were determined by visual inspection using the TVMARK task. Sources affected by ghosts, diffraction spikes, halos from bright sources, and artifacts residing in bright extended emission were rejected. For aperture photometry of the extracted sources, radii of the apertures and inner and outer limits of the sky annuli were selected to be 4.″5, 15″, and 21″, respectively. Magnitudes of the extracted sources were determined using the magnitude zero point of 7.17 Jy provided in the MIPS instrument handbook.[9] Finally, we cross-matched the 24 μm sources with the GLIMPSE catalog using a cone radius of 2″.

Additionally, we have queried the MIPSGAL PSC given by Gutermuth & Heyer (2015). A total of 309 sources are found in the region of interest. Among these sources, 305 are covered by

[8] http://irsa.ipac.caltech.edu/index.html

[9] http://irsa.ipac.caltech.edu/data/SPITZER/docs/mips/

our 24 μm point-source list. The other four sources are weaker than 11.5 MAG. A comparison of the fluxes indicates that our photometry is consistent with that given in Gutermuth & Heyer (2015); the mean difference is smaller than 5% magnitude.

The completeness of our catalog was estimated by counting the number of sources as a function of magnitude. A histogram plot of the source magnitudes in each band was plotted and carefully inspected. The source magnitudes are exponentially distributed. We plot the number of sources in log scale and the magnitude in linear scale, after which we can fit a straight line. The magnitude at which a deviation emerges has been considered as the completeness limit. We found that our catalog is complete to a magnitude of 14.0 at 3.6 μm, 13.5 at 4.5 μm, 12.3 at 5.8 μm, 12.0 at 8.0 μm, and 8.5 at 24 μm. For the central region with diffuse mid-infrared emission, our catalog is complete to a magnitude of 14.0 at 3.6 μm, 13.5 at 4.5 μm, 12.0 at 5.8 μm, 11.5 at 8.0 μm, and 8.0 at 24 μm.

3. RESULTS AND DISCUSSION

In what follows, we separately analyze the physical properties of the H II region G46 (Section 3.1), of the ambient molecular gas (Section 3.2), and of the YSOs near G46 (Section 3.3), with the aim of investigating the impact of the ionizing radiation on the surrounding medium and the likelihood of triggered star formation.

3.1. Exciting Star Candidate(s) and Morphology of G46

A search for the exciting star of G46 in the available OB-type stars catalogs (Reed 2003; Maíz-Apellániz et al. 2004; Maíz-Apellániz et al. 2013) was unsuccessful. However, we can conjecture upon the earliest spectral type of a probable single ionizing star from the radio continuum emission of the H II region. The number of UV ionizing photons needed to keep an H II region ionized is given by $N_{\rm UV} = 0.76 \times 10^{47} T_4^{-0.45} \nu_{\rm GHz}^{0.1} S_\nu D_{\rm kpc}^2$ (Chaisson 1976), where T_4 is the electron temperature in units of 10^4 K, $D_{\rm kpc}$ is the distance in kiloparsecs, $\nu_{\rm GHz}$ is the frequency in GHz, and S_ν is the measured total flux density in Jy. Assuming a typical electron temperature of $T = 10^4$ K, a distance of 4 kpc, and a total flux density of 2.7 Jy as measured from the MAGPIS[10] image at 1.4 GHz, the total amount of ionizing photons needed to keep this source ionized turns out to be about $N_{\rm uv} = (3.5 \pm 1.2) \times 10^{48}$ ph s^{-1}. Assuming errors of about 10% in both distance and radio continuum flux density, we conclude that the exciting star should be an O7V (Martins et al. 2005).

In a rough attempt to identify the star(s) candidate(s) responsible for the ionized gas in the region, we performed an optical and infrared photometric study of the point sources in the area (see Figure 2) based on the astrometric UCAC3 Catalog (Zacharias et al. 2010). Only sources with detections in the optical B and R bands, and in the three near-infrared (NIR) J, H, and K bands extracted from 2MASS,[11] were considered. We found eight sources inside a circle with a size of 4′ centered at the central coordinate of the H II region. Their locations are shown in Figure 2. From the optical and infrared magnitudes, we constructed their spectral energy distribution (SED). We fit the available magnitudes (optical B and R bands, the three JHK 2MASS bands, and the four *Spitzer*-IRAC bands) using the Kurucz photospheric models (Kurucz 1979) included in the tool developed by Robitaille et al. (2007)[12] to obtain the effective temperature, $T_{\rm eff}$, of each source. The fitting tool requires the assumption of the visual extinction, A_v, and the distance. We adopt a distance between 3.5 and 4.5 kpc. Regarding A_v, we derived this value for each source from their $(J–H)$ and $(H–K)$ colors. We assumed the interstellar reddening law of Rieke & Lebofsky (1985; $A_J/A_v = 0.282$, $A_H/A_v = 0.175$, and $A_K/A_v = 0.112$) and the intrinsic colors $(J–H)_0$ and $(H–K)_0$ obtained by Martins & Plez (2006).

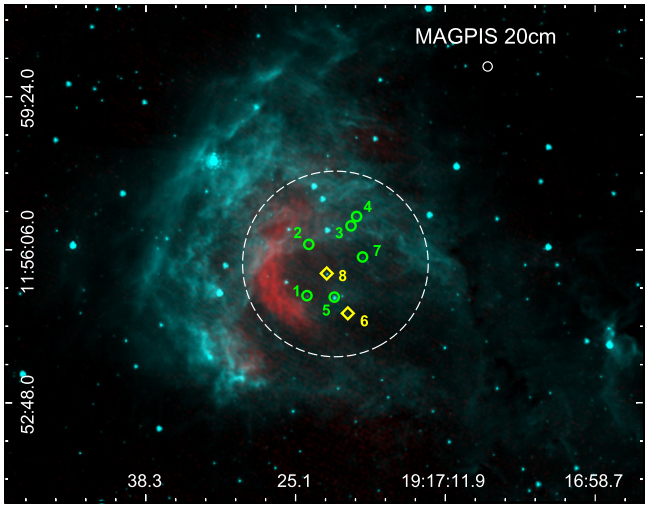

Figure 2. Two-color composite image (8 μm = cyan and 20 cm = red). The symbols represent the only eight point sources with *JHK* near-infrared and RB optical bands measurements found in the region (dashed circle). The diamonds (sources #6 and #8) indicate the location of the most likely candidates to be the exciting stars of G46. The beam of the 20 cm emission from MAGPIS is included in the top right corner.

Among the eight stars found in the region, only three are compatible with a massive star located at the distance of G46. The effective temperatures of the massive candidate stars obtained from the fitting are shown in Table 1. Stars #6 and #8 have $T_{\rm eff}$ of about 30,000 and 35,000 K, respectively, which agree with the temperatures of O9.5V and O7V stars, respectively (Schaerer & de Koter 1997). The models predict an effective temperature of ~26,000 K for source #3, suggesting that this star would be of a spectral type later than B0. The fitted SEDs for sources #6 and #8 are shown in Figure 3. For the remaining sources #1, #2, #4, #5, and #7, Kurucz's models fail to confidently fit their optical and NIR magnitudes as a massive star at about 4 kpc. These sources are probably less massive foreground stars not related to G46. Thus, stars #6 and #8 are the most probable candidates to be the exciting stars of the H II region. Finally, the location of star #8 with respect to the radio continuum emission (red in Figure 2), which looks like an incomplete ring, seems to explain better the curved morphology observed in the ionized gas distribution.

[10] http://third.ucllnl.org/gps/

[11] 2MASS is a joint project of the University of Massachusetts and the Infrared Processing and Analysis Center/California Institute of Technology, funded by the National Aeronautics and Space Administration and the National Science Foundation.

[12] http://caravan.astro.wisc.edu/protostars/

Table 1
Exciting Star Candidate(s) for G46

#	2MASS Designation	J	H	K	B	R	A_v(mag)	$T_{\rm eff}$(K)	$\chi^2_{\rm per\ point}$	Spectral Type
3	19172025+1156369	12.508	12.130	11.942	16.80	14.70	4–5	~26000	1.08	later than B0
6	19172053+1154438	12.498	12.108	11.9815	15.70	14.10	3.5–4.5	~30000	1.28	~O9.5V
8	19172239+1155353	10.094	9.353	8.914	18.40	14.80	4–5	~35000	1.16	~[O7-O7.5]V

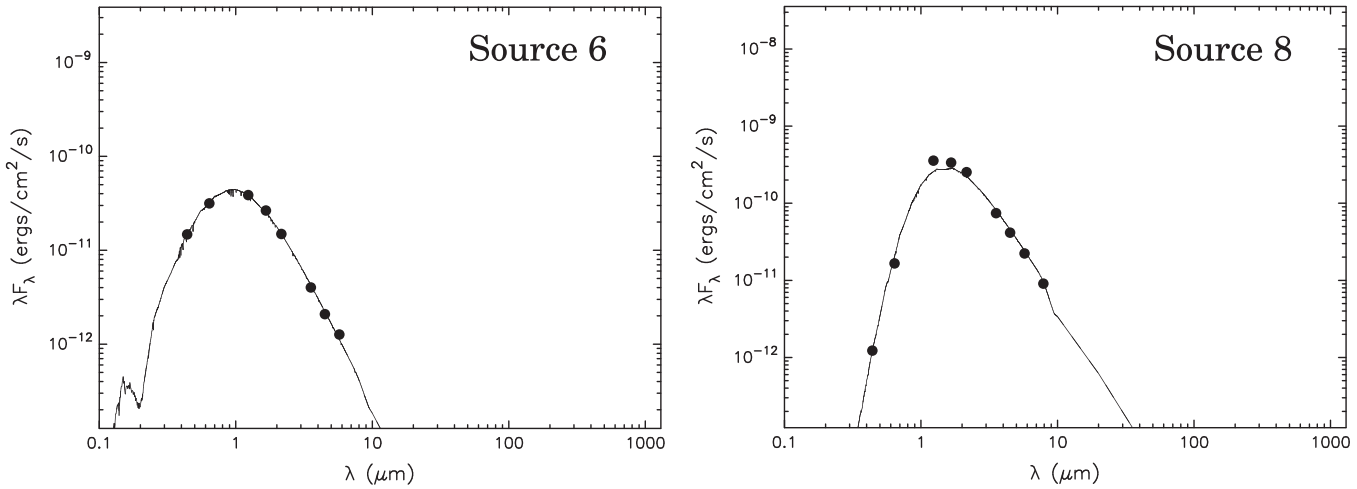

Figure 3. Fitting of the spectral energy distribution for sources #6 and #8. The black curves correspond to the best photospheric model of Kurucz (1979). The dots represent the data used for the fitting.

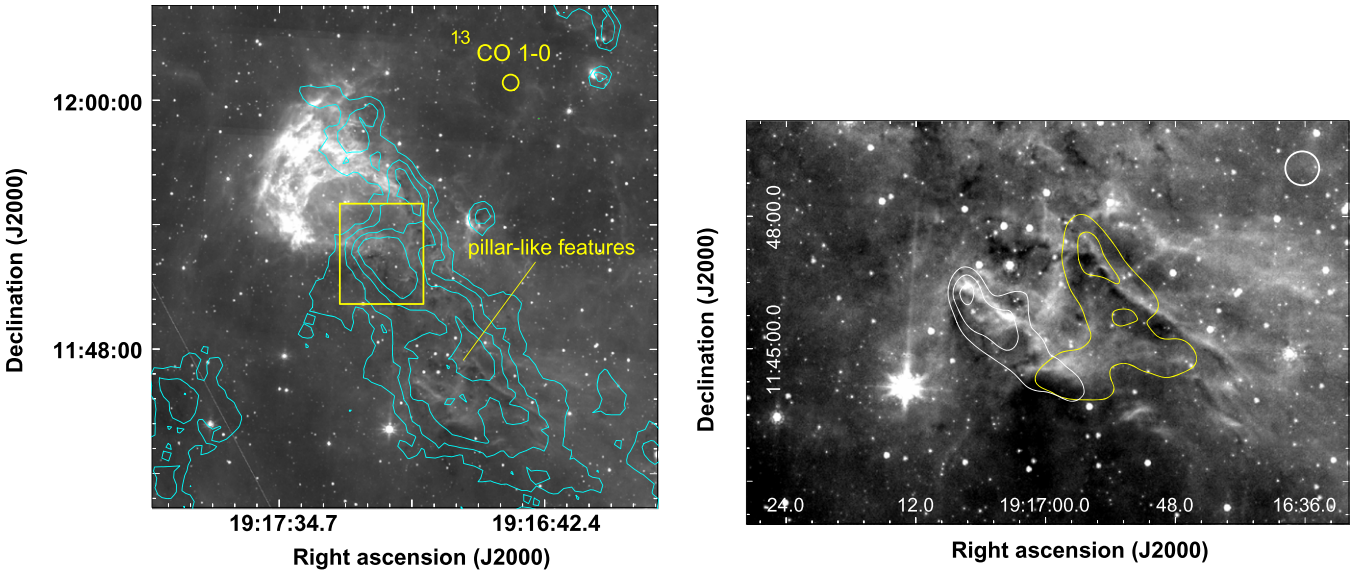

Figure 4. Left: *Spitzer*-IRAC 8 μm emission with contours of the ^{13}CO J = 1–0 emission integrated between 40 and 62 km s^{-1} with levels of 10, 15, 20, and 25 K km s^{-1}. The yellow circle is the beam of the observations. The rms noise is about 1 K km s^{-1}. The rectangle represents the region studied with the JCMT data. Right: integrated ^{13}CO J = 1–0 from the GRS toward the pillar-like features observed in 8 μm. The white contours represent the ^{13}CO emission integrated between 54.0 and 56.5 km s^{-1} with levels of 4.5, 5.0, and 5.5 K km s^{-1}, while the yellow contours represent the integration between 56.5 and 59.0 km s^{-1} with levels of 4 and 5 K km s^{-1}. The beam of the molecular data is shown in the top right corner.

3.2. Molecular Gas Analysis

The H II region G46 is located in projection on a border of the molecular cloud GRSMC G046.34-00.21 cataloged by Rathborne et al. (2009) with an associated $v_{\rm LSR}$ of 54.3 ± 3.9 km s^{-1}. Roman-Duval et al. (2009) established a kinematical distance of about 4 kpc for this molecular cloud, the same as for the H II region G46, supporting both objects being linked. Figure 4 (left) displays the ^{13}CO J = 1–0 integrated emission distribution in the 40–62 km s^{-1} velocity range. It can be seen that the H II region seems to be evolving on the northeastern edge of the cloud. The molecular gas appears to be located in projection onto the diffuse emission at 8 μm observed toward the southwest of the open border of G46. It is noteworthy that there is no evidence of related molecular emission toward the east-northeast edge of the H II region where its associated PAHs emission is thicker and more intense.

The numerous studies of H II regions and their surroundings usually show that the associated PAHs emission is more intense toward the borders of the H II regions with the presence of molecular material. In other words, it is expected that an ionized bubble opens in the direction away from the cloud edge because the ionized gas would be less confined and could stream out into the lower density ISM, forming what is known as a "blister-type" H II region (Israel 1978; Tenorio-Tagle 1979). In the G46 case, however, the ring opens to the southwest, facing the elongated molecular cloud where the density is apparently higher. A possible explanation can be found from the morphology of the G46 radio continuum emission, which suggests a stalling effect for the ionized gas against the photodissociation region (PDR) to the northeast (see Figure 2). This fact suggests that although there is no ^{13}CO $J = 1$–0 detected toward this region, the density of the photodissociated gas is sufficient to confine the ionized gas. The atypical thickness of the PDR toward this edge could be due to the presence of relatively low density gas which is expected toward the edge of a molecular cloud whereby the far-UV photons would have greater penetration in the material. On the other hand, the non-detection of radio continuum emission toward the open border of G46 suggests that the ionized gas escapes from G46 and dilutes in the ISM. The presence of diffuse emission at 8 μm toward the southwest of G46 supports this scenario.

3.2.1. The Pillar-like Features

As mentioned above, about 10′ toward the southwest of the H II region (~12 pc at the assumed distance of 4 kpc), some pillar-like features can be seen emitting at 8 μm, pointing to the ionizing source of G46 and apparently embedded in the molecular cloud GRSMC G046.34-00.21. Even though it seems to be a large distance, several pillars were found as far from the ionizing source as those analyzed in this work (e.g., in the Vulpecula rift; Billot et al. 2010). What is really remarkable in this case is that these pillars-like features, resembling heaps and corrugations, are well outside the H II region, contrary to what is usually found: bubble-like structures with pillars inside or over their boundaries. Taking into account that the pillars point toward the G46 open border, it is suggested that they were produced by UV photons escaping from the H II region.

By inspecting ^{13}CO $J = 1$–0 toward the pillar-like features (Figure 4 (right)), we find that there are two associated molecular structures. The eastern-most IR pillar-like feature has associated molecular gas between 54.0 and 56.5 km s^{-1} (white contours in Figure 4 (right)), while the western one is related to a molecular structure ranging between 56.5 and 59.0 km s^{-1} (yellow contours in Figure 4 (right)). The different velocity ranges for these molecular structures may either indicate that both features are located at slightly different positions along the line of sight or that they have somewhat different kinematics. There is remarkably good agreement between the morphology of the molecular gas and the pillar-like features seen in IR. Moreover, the molecular structures present a morphology consisting of a dense head with a less dense tail, as is usually found by observations toward and predicted by models of this kind of structures in the area surrounding H II regions (Pound et al. 2005, 2007; Schuller et al. 2006). However, following the work of Mackey & Lim (2010), the appearance of these structures resembles a previous evolutionary stage in the formation of pillars because a well-formed tail cannot be identified behind their heads. In what follows, we characterize the interaction between the ionization radiation escaping from G46 and the pillar-like features.

In order to study the radiation influence over the tips of the pillar-like features and the possibilities of triggered star formation via RDI (e.g., Bertoldi 1989; Lefloch et al. 1997; Kessel-Deynet & Burkert 2003), we evaluate the pressure balance between the ionized gas stalling at the head of the pillars and the neutral gas of their interiors. Assuming that the ionizing photons came from an O7V-type star located at the center of G46 (see Section 3.1), we use the predicted ionizing photon flux for an O7V star from Schaerer & de Koter (1997) and the projected distance between the star and the pillars to estimate roughly the amount of UV photons arriving at the surface of the pillars in $\Phi_{\rm pre} \sim 2 \times 10^8$ cm^{-2} s^{-1}. This value represents an upper limit due to the fact that the projected distance between the star and the pillars is a lower limit of the actual distance between them. Our predicted ionizing photon flux is similar to those measured toward several bright-rimmed clouds (Thompson et al. 2004a, 2004b) which, similar to the pillars, are molecular clouds sculpted by the radiation leaking from H II regions, and in many cases they have the same large-scale morphology as the pillars (Thompson et al. 2004a).

Using the $\Phi_{\rm pre}$ obtained above and following Thompson et al. (2004b), we estimate an upper limit for the electron density of about 64 cm^{-3} at the expected ionized boundary layer (IBL) at the tip of both pillar-like structures. This is almost three times greater than the critical value of ~25 cm^{-3} above which an IBL is able to develop around a cloud (Lefloch & Lazareff 1994). To obtain this value, we consider that the pillar heads have radii of 0.5 and assume an effective thickness of the IBL of $\eta = 0.1$. Then, using a typical sound speed for the ionized gas of 11.4 km s^{-1}, we determine that the pillars tips are supporting an external pressure of $P_{\rm ext}/k \sim 2.1 \times 10^6$ cm^{-3} K. It is important to note that the obtained $P_{\rm ext}$ represents strictly an upper limit because the predicted Φ is an upper limit and due to the used η (see Thompson et al. 2004b).

On the other side, integrating the ^{13}CO $J = 1$–0 emission over the area containing each pillar head and using the typical local thermodynamic equilibrium (LTE) formulae to derive the ^{13}CO and H_2 column densities by assuming $T_{\rm ex} = 10$ K and $[H_2/^{13}CO] = 5 \times 10^5$ (see, e.g., Yamaguchi et al. 1999), we estimate the mass of each pillar head to be about 450 and 300 $M_\odot$ for the eastern and western pillars, respectively. The area of each pillar head was assumed taking into account the radius of their tip curvatures, which is a circular area with a radius of 0.5 for both pillar heads. Thus, assuming spherical shapes, we estimate molecular densities of about 7.0×10^3 and 4.6×10^3 cm^{-3}, respectively. Then, considering the velocity interval in which each pillar structure extends, we obtain the velocity dispersion $\sigma_v \sim 1.05$ km s^{-1}, which is in agreement with those predicted by models of pillar formation (Gritschneder et al. 2010; Dale et al. 2012). Finally, using the obtained densities and σ_v, we derive the internal pressure for each pillar head as $P_{\rm int}/k \sim 1.8 \times 10^6$ and $\sim 1.2 \times 10^6$ cm^{-3} K for the eastern and western pillars, respectively. As Thompson et al. (2004b) state, these pressure values are very likely underestimated because the ^{13}CO $J = 1$–0 line underestimates the true density and this molecule may be depleted by selective photodissociation at the boundary of the clouds. Following these authors, the internal pressure is likely underestimated by

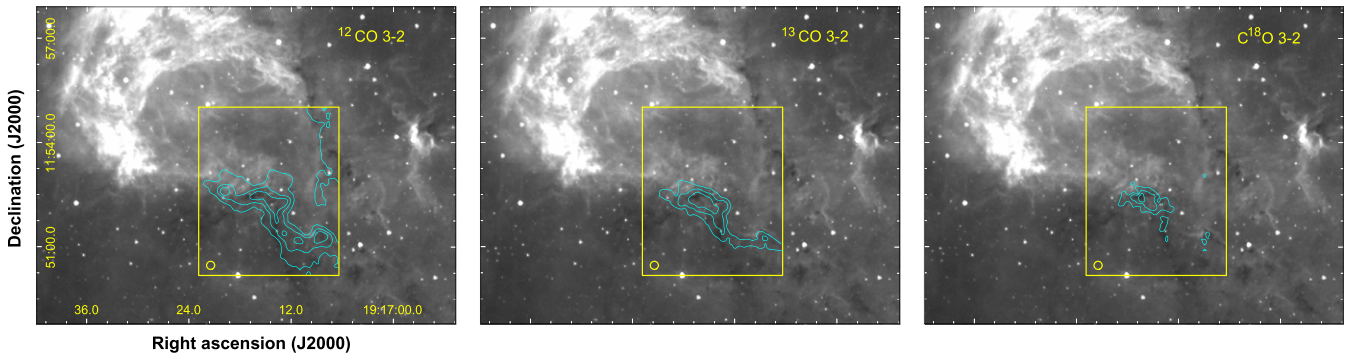

Figure 5. ^{12}CO, ^{13}CO, and C^{18}O $J = 3$–2 emission integrated between 40 and 60 km s^{-1} displayed in contours over the *Spitzer*-IRAC 8 μm emission. The contours levels are 45, 58, and 72 K km s^{-1}; 13, 20, and 27 K km s^{-1}; and 3.3, 5.0, and 6.7 K km s^{-1}, for ^{12}CO, ^{13}CO, and C^{18}O, respectively. The rms noises are about 2.5, 0.8, and 0.5 K km s^{-1}, respectively. The beam of the observations is shown in the bottom left corner of the surveyed region.

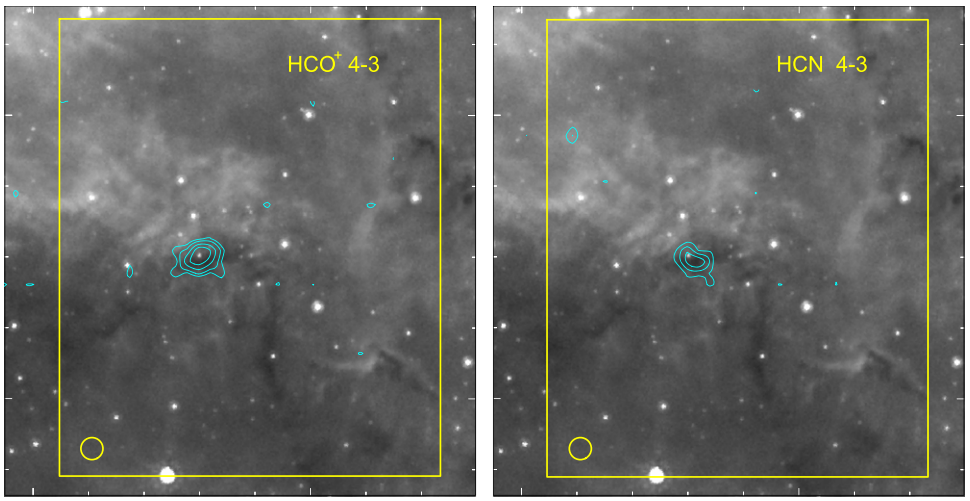

Figure 6. *Spitzer*-IRAC 8 μm emission with contours of the $J = 4$–3 transition of HCO$^+$(left) and HCN (right) integrated between 40 and 65 km s^{-1}. The contours levels are 2.3, 3.3, 5.0, and 8.3 K km s^{-1} for HCO$^+$, and 1.2, 2.0, and 2.8 K km s^{-1} for HCN. The rms noise is about 0.3 K km s^{-1} for both emissions. The yellow rectangle represents the same area as shown in previous figures.

no more than a factor of 15; thus we conclude that $P_{\rm int}/k$ should be between 2×10^6 and 3×10^7 cm^{-3} K.

In conclusion, we obtain $P_{\rm int} > P_{\rm ext}$, which suggests that the diluted ionization front stalls at the pillar heads, probably until the effects of mass evaporation and increasing recombination within the IBL raises the ionized gas pressure to equilibrium with the interior pressure (Lefloch & Lazareff 1994). This result shows that it is unlikely that a shock is propagating farther into the molecular gas, discarding that the RDI mechanism is ongoing in the pillars' interiors.

3.2.2. The Molecular Gas toward G46's Open Border

With the purpose of investigating the molecular material toward the open border of G46, we used higher angular resolution data of several molecular species extracted from the JCMT database acquired toward this region (see the rectangle in Figure 4 (left)). Figure 5 shows the integrated emission of ^{12}CO, ^{13}CO, and C^{18}O $J = 3$–2, while Figure 6 displays the HCO$^+$ and HCN $J = 4$–3 integrated emission. The ^{12}CO and ^{13}CO $J = 3$–2 emission show clumpy, elongated molecular features with a high density filament extending to the southwest of the mapped region. No considerable molecular emission appears toward the open border of G46, suggesting the presence of a pre-existing region with scarce molecular gas, or suggesting that the UV photons have carved the molecular cloud. In any case, this can be the path followed by the UV photons escaping from G46 to reach the farther pillar-like structures.

The C^{18}O $J = 3$–2, HCO$^+$, and HCN $J = 4$–3 emissions are concentrated in a small compact clump related to the infrared dark cloud IRDC 046.424-0.237 (Peretto & Fuller 2009) and to the millimeter continuum source BGPS G046.427-00.237 (see the Bolocam Galactic Plane Survey v2; Ginsburg et al. 2013), suggesting that the emission lines emanate from a deeply embedded clump. Moreover, this structure is associated with the cold high-mass clump G46.43-0.24 (Wienen et al. 2012) in which the (1, 1) and (2, 2) ammonia lines were detected at $v_{\rm LSR} \sim 52.3$ and 52.9 km s^{-1}, respectively. The detection of these molecular species, mainly the HCN $J = 4$–3 line with its critical density that can be between 10^6 and 10^8 cm^{-3} (Takakuwa et al. 2007; Greve et al. 2009), indicates the presence of very high density gas. Considering that this clump is a potential site of star formation, we analyze it in the following.

The line parameters of the observed molecular transitions toward the center of the clump are given in Table 2 as derived from the Gaussian fits from the spectra shown in Figure 7. ^{12}CO $J = 3$–2 was fitted using three Gaussians, while the parameters of the other lines were obtained from single-

Table 2
Line Parameters for the Molecular Lines toward the Center of the Southern Molecular Clump

Molecular Line	T_{mb} Peak (K)	v_{LSR} (km s^{-1})	Δv (FWHM) (km s^{-1})
^{12}CO (3–2)	13.90 ± 0.80	52.50 ± 0.05	2.95 ± 0.15
	1.93 ± 0.33	56.10 ± 0.15	0.95 ± 0.25
	2.92 ± 0.25	58.70 ± 0.30	6.10 ± 0.80
^{13}CO (3–2)	7.83 ± 0.25	52.60 ± 0.01	3.47 ± 0.15
C^{18}O (3–2)	2.75 ± 0.33	51.80 ± 0.15	2.80 ± 0.40
HCO$^+$ (4–3)	2.16 ± 0.15	53.70 ± 0.04	3.15 ± 0.10
HCN (4–3)	0.45 ± 0.12	53.10 ± 0.40	5.50 ± 1.00

component Gaussian fits which coincide in velocity with the main ^{12}CO component. The different velocity components observed in the ^{12}CO spectrum are present over almost the whole region. Thus, we conclude that they correspond to different molecular components along the line of sight, reflecting the clumpiness in the region.

In order to obtain a rough estimate of the molecular clump mass, we assume LTE. We calculate the excitation temperature from

$$T_{ex}(3 \rightarrow 2) = \frac{16.59\ \mathrm{K}}{\ln\left[1 + 16.59\ \mathrm{K}\Big/\left(T_{max}\ (^{12}\mathrm{CO}) + 0.036\ \mathrm{K}\right)\right]}, \quad (1)$$

where T_{max} (^{12}CO) is the ^{12}CO peak temperature toward the clump center at ~52 km s^{-1}, obtaining $T_{ex} \sim 18$ K. We derive the ^{13}CO and C^{18}O optical depths τ_{13} and τ_{18} from (e.g., Buckle et al. 2010)

$$\frac{^{13}T_{mb}}{^{18}T_{mb}} = \frac{1 - \exp(-\tau_{13})}{1 - \exp(-\tau_{13}/X)}, \quad (2)$$

where $^{13}T_{mb}$ and $^{18}T_{mb}$ are the peak temperatures of the ^{13}CO and C^{18}O $J = 3$–2 line at the center of the region, and $X = 8.4$ is the assumed isotope abundance ratio [^{13}CO/C^{18}O] (Frerking et al. 1982; Wilson 1999), providing $\tau_{13} \sim 3.5$ and $\tau_{18} \sim 0.4$, which indicate that the C^{18}O $J = 3$–2 line appears to be moderately optically thin. Thus, we estimate its column density from

$$N\left(\mathrm{C}^{18}\mathrm{O}\right) = 8.26 \times 10^{13} e^{\frac{15.81}{T_{ex}}} \frac{T_{ex} + 0.88}{1 - e^{\frac{-15.81}{T_{ex}}}} \times \frac{1}{J\left(T_{ex}\right) - J\left(T_{BG}\right)} \int T_{mb}\, dv \quad (3)$$

with

$$J(T) = \frac{h\nu/k}{\exp\left(\frac{h\nu}{kT}\right) - 1}. \quad (4)$$

To obtain the molecular hydrogen column density $N(H_2)$, we assume an abundance ratio of $[H_2/C^{18}O] = 5.88 \times 10^6$ (Frerking et al. 1982; Wilson 1999). Finally, the mass was derived from

$$M = \mu m_H \sum_i \left[D^2\, \Omega_i\, N_i\left(H_2\right)\right], \quad (5)$$

where Ω is the solid angle subtended by the beam size, m_H is the hydrogen mass, the mean molecular weight, μ, is assumed to be 2.8 taking into account a relative helium abundance of 25%, and D is the distance. Summation was performed over all of the beam positions on the molecular structure observed in C^{18}O displayed in the contours in Figure 5. The obtained mass is about 375 $M_\odot$. Assuming an ellipsoidal volume with a semi-axis of 45″, 20″, and 20″, we derive a density of $n \sim 1.5 \times 10^4$ cm^{-3}. The density should be higher in the innermost region of the clump where the HCN $J = 4$–3 line emanates, showing a density gradient. Using the deconvolved radius of about 0.5 pc calculated from

$$R_{clump} = \sqrt{\frac{S - \text{beam area}}{\pi}}, \quad (6)$$

where S is the area inside the clump, we note that the mass obtained above is slightly over the mass–size threshold for massive star formation in IRDCs presented in Kauffmann & Pillai (2010), suggesting that massive YSOs can be formed within this clump.

Using the derived HCO$^+$ and HCN $J = 4$–3 parameters listed in Table 2, we performed a non-LTE study of these molecular species with the code RADEX, which uses the mean escape probability approximation for the radiative transfer equation (van der Tak et al. 2007). Using the measured Δv, we ran the code to fit T_{mb} and estimate the column densities. Taking into account that Wienen et al. (2012) measured a kinetic temperature of $T_k \sim 16$ K toward this clump from the ammonia lines, we fix this parameter in 20 K and assume densities between 10^5 and 10^7 cm^{-3} to obtain the values presented in Table 3. From the obtained column densities, we observe HCN/HCO$^+$ abundance ratios of about 4.4, 3.8, and 1.2 for $n_{H_2} = 10^5$, 10^6, and 10^7 cm^{-3}, respectively. In all cases, we obtain a N(HCN)/N(HCO$^+$) ratio larger than unity, as found toward several clumps in IRDC G48.66-0.22 (Pitann et al. 2013) and the active star-forming region W49A (Roberts et al. 2011). As these authors point out, the steady-state chemical models for molecular species in gas-phase predict HCN > HCO$^+$ only for $T_k < 25$ K, with a density of $n_{H_2} = 10^6$ cm^{-3}, which is consistent with our results.

3.3. Star Formation Around G46

Finally, given that the scenario is very favorable for initiating the formation of new generations of stars, in this section we analyze the existence and properties of YSOs in all of the investigated area.

3.3.1. Identification of YSOs

YSOs always show an excess in their infrared emission. The level of excess in the infrared can be effectively used to discriminate YSOs from field stars and distinguishing different evolutionary stages. At a considerably early evolutionary stage, protostars are mostly embedded in dust envelopes and exhibit large excesses of infrared emission and an infrared spectral index $\alpha_{IR} > -0.3$ indicative of flat or ascending SED at wavelengths longward of 2 μm (Lada 1987; Greene et al. 1994). For pre-main-sequence stars which possess optically thick disks, the SEDs tend to descend and the infrared spectral indices are in the range $-1.6 < \alpha_{IR} < -0.3$.

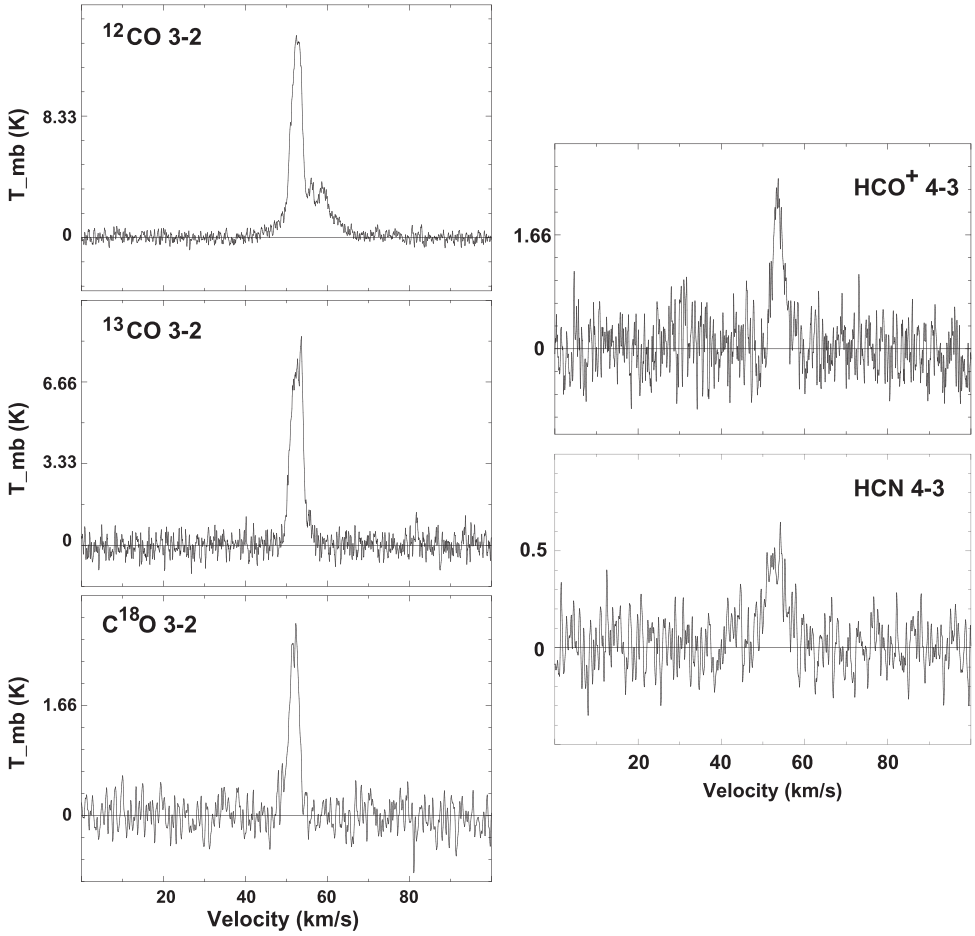

Figure 7. Left: CO isotope spectra. The rms noises of each spectrum are 250, 400, and 200 mK, respectively. Right: HCO^+ and HCN spectra. The rms noises are 33 and 116 mK, respectively. All spectra were obtained toward the center of the dense molecular clump related to IRDC 046.424-0.237 and to the millimeter continuum source BGPS G046.427-00.237.

Table 3
Radex Results from the HCO^+ and HCN $J = 4$–3 Lines using $T_k = 20$ K and the Indicated n_{H_2}

Input n_{H_2} (cm^{-3})	$N(HCO^+)$ (cm^{-2})	τ_{HCO^+}	N(HCN) (cm^{-2})	τ_{HCN}	X_{HCN/HCO^+}
10^5	1.9×10^{14}	7.50	8.4×10^{14}	4.50	4.42
10^6	1.7×10^{13}	0.70	6.5×10^{13}	0.37	3.82
10^7	5.4×10^{12}	0.14	6.8×10^{12}	0.09	1.25

Finally "transition disk" sources are more evolved YSOs where the inner parts of the disks have been cleared by photoevaporation of the central stars or by planet forming processes. For such YSOs, we expect to detect IR excesses at wavelengths longer than 16 μm (Strom et al. 1989). These properties of YSOs make photometric observations in the near- to mid-infrared plausible mechanisms for discriminating them from field stars. Different color-based source identification and classification schemes have been developed and verified in practice. In this section, we identify potential YSOs following the scheme proposed by Gutermuth et al. (2009). The resulting YSOs are classified as Class I (protostars, including Class 0, Class I, and "flat spectrum" sources), Class II, and "transition disk" sources.

There are several kinds of contaminants that could be misidentified as YSOs in our original sample. Extragalactic contamination could stem from star-forming galaxies and broad-line active galactic nuclei, which show PAH emission features yielding very red 5.8 and 8.0 μm colors (Stern et al. 2005; Gutermuth et al. 2008). In our own Galaxy, unresolved knots of shock emission and resolved PAH emission are often detected in the IRAC bands, yielding additional contaminants. Following the techniques presented in Gutermuth et al. (2009), we exclude contaminants, and then identify and categorize potential YSOs as described in the following.

In the first phase, only sources with valid detections in all four IRAC bands were considered. Any source fulfilling the color criteria of $[3.6] - [4.5] > 0.7$ and $[4.5] - [5.8] > 0.7$ is regarded as a Class I YSO. In the remaining pool, Class II sources were picked out based on the constraints of (i) $[3.6] - [4.5] - \sigma_1 > 0.15$, (ii) $[3.6] - [5.8] - \sigma_2 > 0.35$, (iii) $[4.5] - [8.0] - \sigma_3 > 0.5$, and (iv) $[3.6] - [5.8] + \sigma_2 \leqslant \frac{0.14}{0.04} \times (([4.5] - [8.0] - \sigma_3) - 0.5) + 0.5$. Here, $\sigma_1 = \sigma([3.6] - [4.5])$, $\sigma_2 = \sigma([3.6] - [5.8])$, and $\sigma_3 = \sigma([4.5] - [8.0])$ are combined errors added in quadrature.

In the second phase, sources with 24 μm data in the remaining pool are re-examined. Sources with colors of $[5.8] - [24] > 2.5$ or $[4.5] - [24] > 2.5$ are classified as "transition disks." With the potential contaminants and YSOs identified above excluded, there still remain some sources with

Table 4
Source Counts in the YSO Search

Sources	G46 Field
In GLIMPSE Catalog	19210
Valid in all Four IRAC Bands[a]	4491
With 24 μm data	338
Rejected Contaminants	883
Class I Type	22
Class II Type	60
Transition Disks	24
Total YSO Candidates	106

Note.
[a] Sources with photometric uncertainties no larger than 0.2 mag in all four IRAC bands.

bright 24 μm emission. For sources lacking valid photometric data in one or more of the IRAC bands, these are picked out as additional Class I YSOs once fulfilling $[24] > 7$ and $[X] - [24] > 4.5$ MAG, where $[X]$ is the longest wavelength IRAC detection that we have.

The classification scheme of Gutermuth et al. (2009) includes three phases, using 2MASS data to identify more YSOs in addition to the aforementioned methods. However, in our case, as G46 is much farther than the sources in Gutermuth et al. (2009), 2MASS photometry would be severely affected by foreground interstellar extinction, and the use of these near-IR data to identify YSOs would induce heavy contamination from foreground field stars. Thus, we do not use the NIR bands in our YSOs search.

The above identification procedures have resulted in 106 YSOs. They are classified into 22 Class I, 60 Class II, and 24 "transition disks" objects. A summary of the results is given in Table 4. We note that the color-based classification scheme would lead to misidentification. A Class II YSO viewed at high inclination would show features resembling those of a Class I source. An edge-on Class I YSO can have infrared color similar to a Class 0 source. Thus, all Class I, II, and "transition disk" sources identified in this paper are YSO candidates. The distribution of these YSO candidates on distinct color–color spaces are presented in Figures 8 and 9. It is important to note that we also use the point sources extracted from Gutermuth & Heyer (2015) to identify YSO candidates and reach identical results.

3.3.2. Active Star Formation in GRSMC G046.34-00.21

Figure 10(a) shows the large-scale spatial distribution of the 106 YSOs identified in the region. Among the 82 Class I and Class II YSOs, more than 40 (about 50%) are located in projection onto the molecular cloud GRSMC G046.34-00.21 (see Figure 4), which fills only the 20% of the whole survey field. Such a concentration of YSOs is suggestive of active star formation taking place in the cloud. On the other hand, from the 24 "transition disks" found in the whole field, none are detected associated with the molecular gas, indicating the relatively young nature of the YSOs embedded in this cloud. Interestingly, all of the YSOs associated with the molecular cloud are placed in projection between the open border of G46 and the head of the pillars. Moreover, there are no young sources in the farthest part of the cloud behind the heads of these pillars (see Figure 10(b)).

From Figure 10(a), only two concentrations of young objects can be noted over the whole field, one centered at $19^h16^m30^s$, $+11°51'00''$ (J2000), consisting of 15 Class II type sources, and the other centered at $19^h17^m00^s$, $+11°47'00''$ (J2000) mostly composed by Class I type YSOs (nine sources), which are located just ahead of the pillar-like features. A closeup view of the pillar-like feature regions is shown in Figure 10(b). A point source is revealed at 24 μm which is too faint in the IRAC bands and not listed in the GLIMPSE catalog. We have marked this 24 μm point source using a red circle in Figure 10(b). Weak at short wavelengths, this point source would be younger than the others and could be a Class 0 candidate.

The fact that the Class II concentration is located closer to the open border of G46 than the Class I group strongly suggests an age gradient in the YSO distribution. On the other hand, the absence of young sources inside and behind the pillar-like structures could indicate that the H II region's influence has not reached the molecular material behind the pillars, which is in agreement with the result of Section 3.2.1. We suggest a scenario in which the propagation of ionization radiation escaping from the H II region triggered the star formation observed in the molecular cloud through an RDI mechanism and then stalled at the surface of the pillars heads. We cannot discount that a growing density of the IBL reaches equilibrium with that of the cloud, and thus the shock front will continue its propagation into the cloud (Thompson et al. 2004a).

Additionally, in the region surveyed with JCMT (see yellow rectangle in Figure 4), there are five YSO candidates. One of these candidates, a Class I source, lies exactly at the center of the dense molecular clump mapped with HCO^+ and HCN $J = 4$–3 (see Figure 6), which is in agreement with the molecular gas conditions studied in Section 3.2.2.

4. CONCLUSIONS

We analyzed the H II region G46.5-0.2, its molecular environment, and the YSOs in a wide region around it, searching for evidence of their physical connection and the possibility of induced star formation. We found a rich combination of mutual influences, underscoring the important role of H II regions for the formation of new stars, not only in the immediate vicinity but also farther than a distance equivalent to its own radius.

We characterized that the H II region, located at about 4 kpc and with a radius of ~4.6 pc, is probably excited by an O7V star. Its shape resembles a horse shoe with a bright, thick border toward the east-northeast and an open portion toward the southwest. While mapping the distribution of the molecular gas associated with G46, we found that the H II region is located close to the edge of the GRSMC G046.34-00.21 molecular cloud and, curiously, instead of opening in the direction of lower ambient density, G46 does so in exactly the opposite direction, toward the cloud. Filamentary structure in the molecular cloud is observed, particularly in the ^{12}CO $J = 3$–2 and ^{13}CO $J = 3$–2 maps. Toward the open border of G46 there does not appear to be any considerable molecular emission, suggesting the presence of a pre-existing region with scarce molecular gas or suggesting that the UV photons have carved the molecular cloud. Also, close to the end of the observed filamentary structures in the cloud, the infrared images reveal the existence of pillar-like structures pointing toward the H II region open border which are associated with

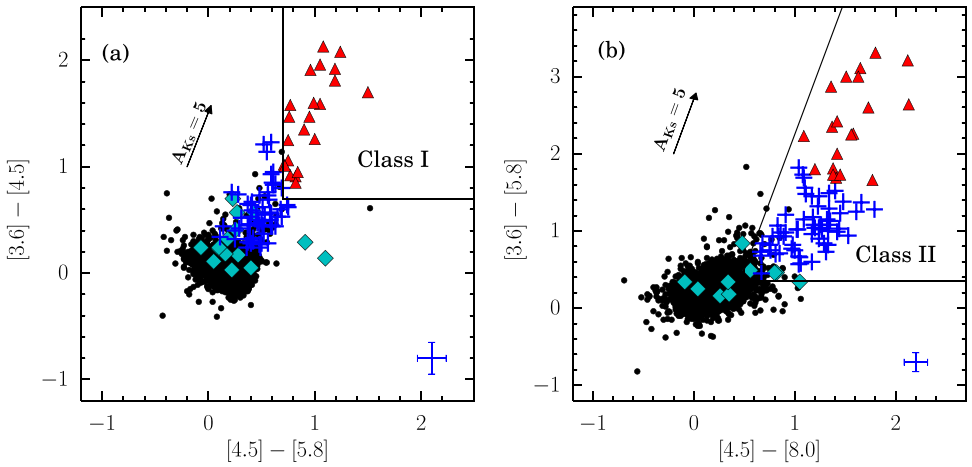

Figure 8. IRAC color–color diagrams. Class I, Class II, and "transition disk" YSOs are marked using red triangles, blue plus symbols, and cyan diamonds, respectively. Mean errors of colors are presented in the bottom right corner of each panel. The definition of loci are adopted from Gutermuth et al. (2009).

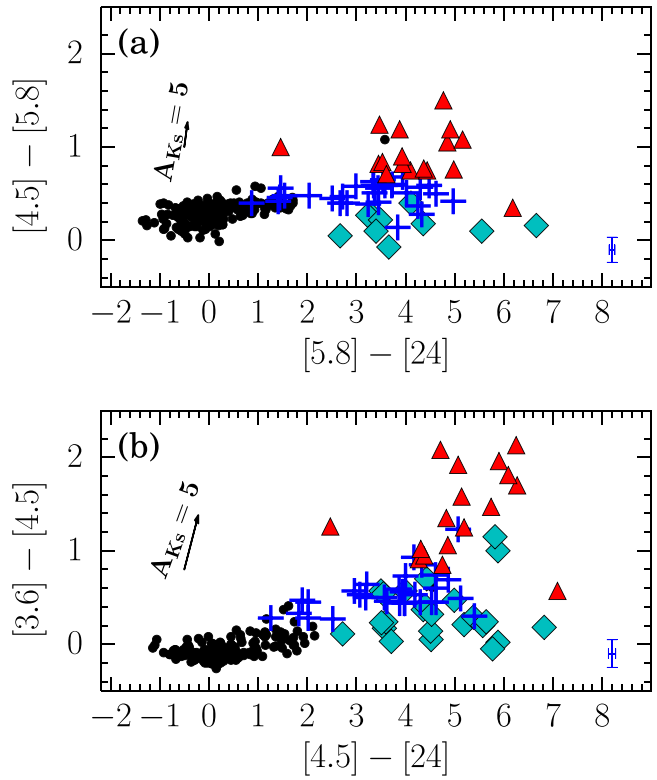

Figure 9. IRAC-MIPS color–color diagrams. Class I, Class II, and "transition disk" YSOs are marked using red triangles, blue plus symbols, and cyan diamonds, respectively. Mean errors of colors are presented in the bottom right corner of each panel.

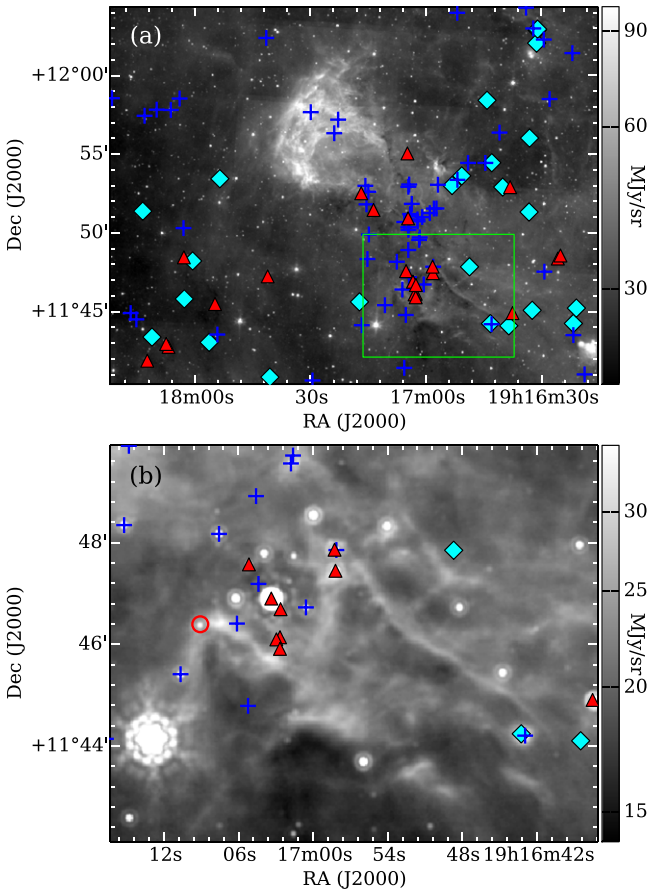

Figure 10. (a) Distribution of YSOs. Class I, Class II, and "Transition Disk" YSOs are marked using red triangles, blue plus symbols, and cyan diamonds, respectively. The grayscale shows emission at 8.0 μm. (b) A closeup view of the pillar-like features region. The background presents emission at 24 μm.

some narrow molecular filaments characterized using the ^{13}CO $J = 1$–0 line. From a pressure balance study, we found that the internal pressure of the neutral gas in the pillar-like feature heads are larger than the external pressure due to the ionized gas stalling at their tips, discarding the possibility that the RDI mechanism is ongoing. In addition, we analyzed a compact molecular clump located over the south border of G46, obtaining a mass of $\sim 375\,M_{\odot}$ and a density of about $10^4\,\mathrm{cm}^{-3}$ with a higher density toward its center where the HCN $J = 4$–3 line is detected.

Taking into account the expansion of the H II region itself, and that the injection of extra energy into the molecular cloud can drive turbulence and trigger star formation, we searched for candidate YSOs and classified them according to their evolutionary stage. We identified two main concentrations of young objects over the whole region, one closer to the G46 open border consisting of Class II type sources, and another mostly composed of Class I type YSOs located just ahead of the pillar-like features, strongly suggesting an age gradient in the YSOs distribution.

We thank the anonymous referee for useful comments and corrections. S.P., M.O., G.D., A.P., and E.G. are members of the *Carrera del Investigador Científico* of CONICET, Argentina. G.D. acknowledges hospitality from the National Astronomical Observatories (Chinese Academy of Sciences) in Beijing. This work was partially supported by Argentinian grants awarded by CONICET, ANPCYT, and UBA (UBA-CyT). This work is partially supported by the China Ministry of Science and Technology through grant of 2010DFA02710 (the China-Argentina Radio Telescope project) and NSFC through grants of 110732027, 11373009, 11433008, and 11403040. J.-H.Y. and Y. F.H. are supported by the Young Research Grant of NAOC.

REFERENCES

Anderson, L. D., & Bania, T. M. 2009, ApJ, 690, 706
Benjamin, R. A., Churchwell, E., Babler, B. L., et al. 2003, PASP, 115, 953
Bertoldi, F. 1989, ApJ, 346, 735
Billot, N., Noriega-Crespo, A., Carey, S., et al. 2010, ApJ, 712, 797
Buckle, J. V., Curtis, E. I., Roberts, J. F., et al. 2010, MNRAS, 401, 204
Buckle, J. V., Hills, R. E., Smith, H., et al. 2009, MNRAS, 399, 1026
Carey, S. J., Noriega-Crespo, A., Mizuno, D. R., et al. 2009, PASP, 121, 76
Chaisson, E. J. 1976, in Frontiers of Astrophysics, ed. E. H. Avrett (Cambridge, MA: Harvard Univ. Press), 259
Dale, J. E., Ercolano, B., & Bonnell, I. A. 2012, MNRAS, 424, 377
Deharveng, L., Lefloch, B., Kurtz, S., et al. 2008, A&A, 482, 585
Dirienzo, W. J., Indebetouw, R., Brogan, C., et al. 2012, AJ, 144, 173
Elmegreen, B. G., Kimura, T., & Tosa, M. 1995, ApJ, 451, 675
Fazio, G. G., Hora, J. L., Allen, L. E., et al. 2004, ApJS, 154, 10
Frerking, M. A., Langer, W. D., & Wilson, R. W. 1982, ApJ, 262, 590
Ginsburg, A., Glenn, J., Rosolowsky, E., et al. 2013, ApJS, 208, 14
Greene, T. P., Wilking, B. A., Andre, P., Young, E. T., & Lada, C. J. 1994, ApJ, 434, 614
Greve, T. R., Papadopoulos, P. P., Gao, Y., & Radford, S. J. E. 2009, ApJ, 692, 1432
Gritschneder, M., Burkert, A., Naab, T., & Walch, S. 2010, ApJ, 723, 971
Gutermuth, R. A., & Heyer, M. 2015, AJ, 149, 64
Gutermuth, R. A., Megeath, S. T., Myers, P. C., et al. 2009, ApJS, 184, 18
Gutermuth, R. A., Myers, P. C., Megeath, S. T., et al. 2008, ApJ, 674, 336
Israel, F. P. 1978, A&A, 70, 769
Jackson, J. M., Rathborne, J. M., Shah, R. Y., et al. 2006, ApJS, 163, 145
Kauffmann, J., & Pillai, T. 2010, ApJL, 723, L7
Kessel-Deynet, O., & Burkert, A. 2003, MNRAS, 338, 545
Kurucz, R. L. 1979, ApJS, 40, 1
Kuchar, T. A., & Bania, T. M. 1994, ApJ, 436, 117
Lada, C. J. 1987, in IAU Symp. 115, Star Forming Regions, ed. M. Peimbert & J. Jugaku (Dordrecht: Reidel), 1
Lefloch, B., & Lazareff, B. 1994, A&A, 289, 559
Lefloch, B., Lazareff, B., & Castets, A. 1997, A&A, 324, 249
Lockman, F. J. 1989, ApJS, 71, 469
Mackey, J., & Lim, A. J. 2010, MNRAS, 403, 714
Maíz-Apellániz, J., Walborn, N. R., Galué, H. Á, & Wei, L. H. 2004, ApJS, 151, 103
Maíz Apellániz, J., Sota, A., Morrell, N. I., et al. 2013, in Proc. of 10th Meeting of Massive Stars, Massive Stars: From Alpha to Omega, 198
Martins, F., & Plez, B. 2006, A&A, 457, 637
Martins, F., Schaerer, D., & Hillier, D. J. 2005, A&A, 436, 1049
Ortega, M. E., Paron, S., Giacani, E., Rubio, M., & Dubner, G. 2013, A&A, 556, A105
Panagia, N. 1973, AJ, 78, 929
Paron, S., Petriella, A., & Ortega, M. E. 2011, A&A, 525, A132
Peretto, N., & Fuller, G. A. 2009, A&A, 505, 405
Pitann, J., Linz, H., Ragan, S., et al. 2013, ApJ, 766, 68
Pound, M. W., Kane, J. O., Remington, B. A., et al. 2005, Ap&SS, 298, 177
Pound, M. W., Kane, J. O., Ryutov, D. D., Remington, B. A., & Mizuta, A. 2007, Ap&SS, 307, 187
Quireza, C., Rood, R. T., Balser, D. S., & Bania, T. M. 2006, ApJS, 165, 338
Rathborne, J. M., Johnson, A. M., Jackson, J. M., Shah, R. Y., & Simon, R. 2009, ApJS, 182, 131
Reed, B. C. 2003, AJ, 125, 2531
Rieke, G. H., & Lebofsky, M. J. 1985, ApJ, 288, 618
Rieke, G. H., Young, E. T., Engelbracht, C. W., et al. 2004, ApJS, 154, 25
Roberts, H., van der Tak, F. F. S., Fuller, G. A., Plume, R., & Bayet, E. 2011, A&A, 525, A107
Robitaille, T. P., Whitney, B. A., Indebetouw, R., & Wood, K. 2007, ApJS, 169, 328
Roman-Duval, J., Jackson, J. M., Heyer, M., et al. 2009, ApJ, 699, 1153
Schaerer, D., & de Koter, A. 1997, A&A, 322, 598
Schuller, F., Leurini, S., Hieret, C., et al. 2006, A&A, 454, L87
Skrutskie, M. F., Cutri, R. M., Stiening, R., et al. 2006, AJ, 131, 1163
Stern, D., Eisenhardt, P., Gorjian, V., et al. 2005, ApJ, 631, 163
Stetson, P. B. 1987, PASP, 99, 191
Strom, K. M., Strom, S. E., Edwards, S., Cabrit, S., & Skrutskie, M. F. 1989, AJ, 97, 1451
Takakuwa, S., Ohashi, N., Bourke, T. L., et al. 2007, ApJ, 662, 431
Tenorio-Tagle, G. 1979, A&A, 71, 59
Thompson, M. A., Urquhart, J. S., & White, G. J. 2004b, A&A, 415, 627
Thompson, M. A., White, G. J., Morgan, L. K., et al. 2004a, A&A, 414, 1017
Tremblin, P., Minier, V., Schneider, N., et al. 2013, A&A, 560, A19
van der Tak, F. F. S., Black, J. H., Schöier, F. L., Jansen, D. J., & van Dishoeck, E. F. 2007, A&A, 468, 627
Werner, M. W., Uchida, K. I., Sellgren, K., et al. 2004, ApJS, 154, 309
Wienen, M., Wyrowski, F., Schuller, F., et al. 2012, A&A, 544, A146
Wilson, T. L. 1999, RPPh, 62, 143
Yamaguchi, R., Saito, H., Mizuno, N., et al. 1999, PASJ, 51, 791
Zacharias, N., Finch, C., Girard, T., et al. 2010, AJ, 139, 2184
Zavagno, A., Anderson, L. D., Russeil, D., et al. 2010, A&A, 518, L101

The Astronomical Journal, 154:40 (1pp), 2017 July https://doi.org/10.3847/1538-3881/aa7b8b

Erratum: "H II Region G46.5-0.2: The Interplay between Ionizing Radiation, Molecular Gas, and Star Formation" (2015, AJ, 149, 193)

S. Paron[1,2], M. E. Ortega[1], G. Dubner[1], Jing-Hua Yuan[3], A. Petriella[1], E. Giacani[1,2], Jin Zeng Li[3], Yuefang Wu[4], Hongli Liu[3], Ya Fang Huang[3], and Si-Ju Zhang[3]
[1] CONICET-Universidad de Buenos Aires. Instituto de Astronomía y Física del Espacio, CC 67, Suc. 28, 1428 Buenos Aires, Argentina; sparon@iafe.uba.ar
[2] Universidad de Buenos Aires. Facultad de Arquitectura, Diseño y Urbanismo. Buenos Aires, Argentina
[3] National Astronomical Observatories, Chinese Academy of Sciences, 20A Datun Road, Chaoyang District, Beijing 100012, China
[4] Department of Astronomy, Peking University, 100871 Beijing, China
Received 2017 June 23; published 2017 July 5

In the published paper, in Section 3.2.1, the masses of the pillar heads were overestimated as a consequence of the use of an area larger than the area actually occupied by each head. The actual values are about 80 and 60 $M_{\odot}$ for the eastern and western pillar heads, respectively. The densities in the pillar heads do not change significantly; they are still a few 10^3 cm^{-3}. Hence, the analysis of pressure balance in the radiative driven implosion context remains the same, with the same conclusions.